Accurate malocclusion tooth segmentation method based on a level set with adaptive edge feature enhancement

Shuyi Jiang [a], Han Zhang [b], Zhi Mao [b], Yonghui Li [a], Guanyuan Feng [a],[*],[1]

[a] *College of Computer Science and Technology, Changchun University of Science and Technology, Changchun, 130012, China*
[b] *Department of Orthodontics, Jilin University Stomatology Hospital, Changchun, 130021, China*

A B S T R A C T

Objective: This study aimed to accurately segment teeth under complex oral conditions, including complex structural interference among adjacent teeth or malocclusion conditions, such as tooth rotation and displacement caused by dental crowding.
Study design: Cone-beam computed tomography (CBCT) images were obtained from 19 patients with complex oral conditions, and a three-step solution was proposed. This study used a global convex level-set model to extract bony tissue and developed a flexible curve extraction method for separating neighbouring teeth under complex structural interference. In addition, a local level-set model with adaptive edge feature enhancement was proposed to segment individual teeth precisely. This model adaptively enhances edge features based on the structure of the root boundary and accurately distinguishes between the close-contact root and alveolar bone resulting from tooth rotation or displacement.
Results: The experimental results showed that the average Dice similarity coefficient values for incisors, canines, premolars, and molars were 93.30%, 93.47%, 93.24%, and 93.89%, respectively, and the average tooth centroid distances were 0.66, 0.61, 0.87, and 0.80 mm, respectively.
Conclusion: The proposed method can effectively segment teeth without relying on highly precise annotated datasets, yielding satisfactory results even under complex structural interference between adjacent teeth or tooth rotation and displacement caused by dental crowding. It is more robust than the other methods and provides valuable data for further research and clinical practice.

1. Introduction

With computer technology and many orthodontic oral subjects of crossover and integration, digital oral diagnosis and treatment provide a more precise and personalised healthcare experience and digital dental model for patients and doctors, which are vital in clinical practice [1–3]. A complete digital dental model includes soft and hard tissues, such as crowns, roots, jawbones, and gingiva. Using the digital model data of soft and hard tissues, orthodontists can accurately simulate and design tooth movement, evaluate the relationship between the root and bone, and assess the risks of bone dehiscence and fenestration. Compared with traditional

orthodontics, digital technology applications dramatically increase the predictability of treatment outcomes and effectively control risks. Currently, with the popularisation of oral and model scanning equipment, doctors can easily obtain digital models of crowns and gingiva. The establishment of a root model relies on the collection of CBCT images. Cone-beam computed tomography (CBCT) images are widely used in the diagnosis and treatment of oral and maxillofacial diseases because of their low radiation doses, high isotropic spatial resolution, and complete root data. The uniqueness of this data source makes tooth segmentation in the CBCT data crucial for establishing a complete digital model.

Researchers have proposed several methods for complete tooth segmentation, which can be divided into two types: direct 3D segmentation and 2D slice-by-slice segmentation. Methods based on direct 3D segmentation include a rapid automatic segmentation method based on a region-growth algorithm that involves four predefined thresholds [4]. However, growth regions may not be distinguishable from a predefined threshold because of their similar intensities in images of the alveolar bone or other tissues in and around the root [5]. In Refs. [6,7], a 3D region-based level-set method was applied for tooth segmentation. However, tooth segmentation guided by only global intensity statistics cannot accurately distinguish between the tooth root and the alveolar bone with similar image intensities. Although the application of a 3D level-set approach can effectively achieve tooth segmentation in most cases, it lacks local control. In a 2D slice-by-slice-based segmentation approach, an optimal thresholding method for tooth segmentation based on the superstructure and image intensity information was proposed [8], which was superior to global thresholding. However, the structure of a tooth is too complex to achieve satisfactory results using a single threshold. Inspired by the significant success of deep learning in computer vision and medical image computing in recent years, an increasing number of researchers have begun building neural networks [9–15]. Although methods that learn the feature information of objects for prediction have achieved satisfactory results, they encounter the problem of a lack of high-quality datasets. Studies on weakly supervised learning techniques require only a rough label [16,17], but their accuracy is poor. The level-set method performs better in tooth segmentation than other traditional segmentation models [5,18–23]. Xia et al. [29] proposed a segmentation line based on the Radon transform to separate neighbouring teeth, achieving independent segmentation of each tooth. Their experiments focused on the segmentation of neatly arranged, structurally stable teeth. However, patients who require CBCT imaging often have various dental problems, including complex structural interference between adjacent teeth, tooth rotation, and displacement caused by dental crowding. Therefore, this remains a challenging task in clinical practice for the following reasons:

(1) The presence of impacted teeth or other structurally complex dental conditions in CBCT images can result in complex structural interference with adjacent teeth. Traditional methods for separating neighbouring teeth cannot accurately segment adjacent teeth under such conditions, compromising precision and making it challenging for doctors to accurately observe neighbouring tooth boundaries, potentially affecting subsequent diagnosis.
(2) Tooth rotation and displacement caused by dental crowding can result in excessive contact between the tooth roots and alveolar bone, resulting in the loss of their boundaries in CBCT images. Because teeth and alveolar bone have similar intensities in the images, traditional tooth segmentation methods can only differentiate between non-tightly contacted root and alveolar bone. This may result in the root of the reconstructed 3D dental model not being enveloped by alveolar bone, further causing deviations in doctors' judgment of the alveolar bone's shape and the anatomical position relationship with the root, thereby increasing the corresponding risk of orthodontic treatment.
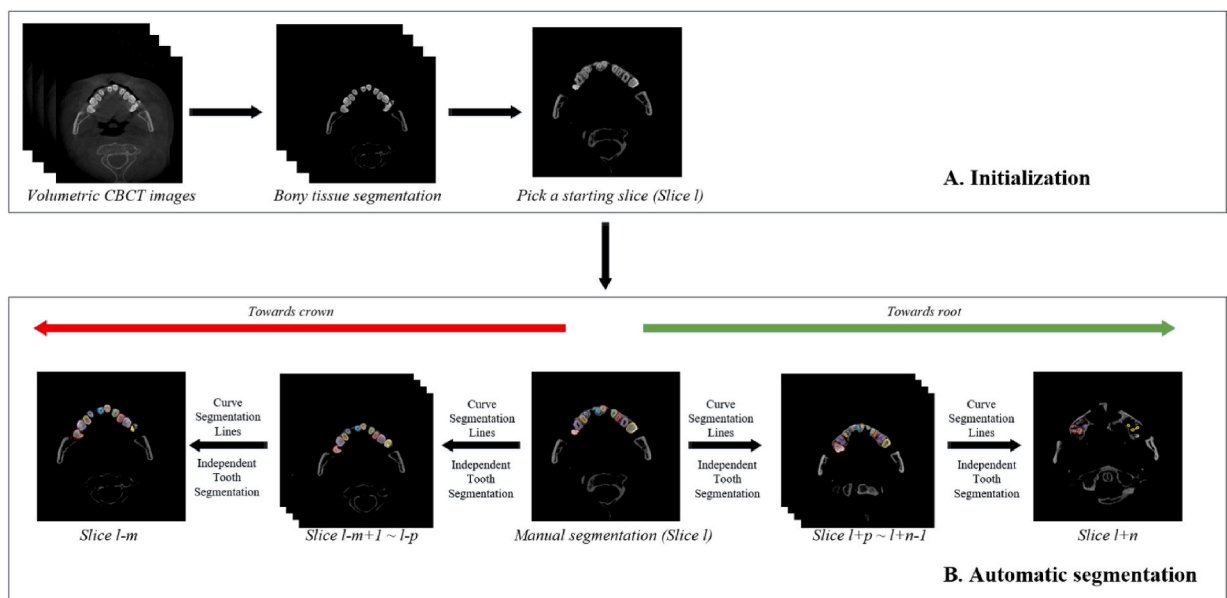

Fig. 1. Slice-by-slice tooth segmentation flowchart.

This study aimed to achieve precise tooth segmentation in CBCT images under complex oral conditions, such as complex structural interference between adjacent teeth or tooth rotation and displacement, without heavy reliance on extensively annotated datasets. A flexible and curved segmentation line was created for the precise separation of neighbouring teeth with complex structural interference, followed by the segmentation of each tooth. Considering the close contact between tooth roots and alveolar bone caused by tooth rotation or displacement, this study developed a hybrid level-set model with adaptive edge feature enhancement, which can enhance the boundary features to varying degrees based on the structure at the root boundary. Two optimization coefficients were constructed to optimise the edge indicator, enabling the level-set curve to accurately guide the differentiation between the tooth root and the surrounding alveolar bone, thus achieving high-precision tooth segmentation in scenarios such as tooth rotation and displacement. In summary, the proposed method is simple and effective and does not rely on many annotated datasets. It can adapt to complex oral conditions and is more robust than the other methods, the workflow is shown in Fig. 1.

2. Methods and materials

In this study, 19 CBCT images were selected for the segmentation experiments. The scanning (NewTom VG, Italy) parameters of the CBCT images evaluated were 120 kV, 5 mA, with an exposure time of 6 s. The field of view (FOV) was 8 or 12 cm, the voxel size was 0.25 mm, and the file format was DICOM. We initially excluded cases with metal braces and metal restorations and included cases involving teeth with mild to moderate crowding (with a difference of approximately 2–9 mm between the dental arch length and dental arch curve length). Additionally, within the dataset, there were complex structural interference data related to impacted teeth and adjacent teeth. All data were used after obtaining informed consent from the patients.

The experimental data type was professionally assessed by experienced orthodontists from the Jilin University Stomatology Hospital, and the algorithm results were compared with the manual segmentation results of experienced doctors, which served as the gold standard.

2.1. Global convex segmentation model for bony tissue separation

Because regions composed of non-bony tissue (soft tissue and air) do not require segmentation, they are considered as background. Therefore, the first task in this study was to separate the bony tissue through the convex segmentation of CBCT images. As shown in Equation (1), a hybrid active contour model is adopted in this paper based on the Chan–Vese and local binary fitting (LBF) models [24–26].

$$E_{global} = \omega E_{CV} + (1 - \omega)E_{LBF} + E_{edge} \tag{1}$$

With the Chan–Vese model (E_{CV}) in (1), an image segmentation method based on global energy minimisation was represented as $\int_{\Omega} \lambda_1 \cdot |I(y) - c_1|^2 H_{\varepsilon}(\varphi) + \lambda_2 \cdot |I(y) - c_2|^2 (1 - H_{\varepsilon}(\varphi))dy$. A global energy function was used to describe the foreground and background areas of an image, which are indicated by c_1 and c_2 in (1), respectively. Specifically, the Chan–Vese model divides an image into foreground and background regions. In this study, the foreground was represented as bony tissue and the background was defined as non-bony tissue. The segmentation results were determined by minimising the global energy function. In contrast, the LBF model (E_{LBF}) in (1) was represented as $\int_{\Omega} \lambda_1 \cdot |I(y) - f_1|^2 H_{\varepsilon}(\varphi) + \lambda_2 \cdot |I(y) - f_2|^2 (1 - H_{\varepsilon}(\varphi))dy$. Unlike the Chan–Vese model, the LBF model is an image segmentation method based on a local binary mode. Specifically, the LBF model divides each image into several small regions, calculates the local binary mode in each small region, and determines the segmentation result based on the relationship between the local binary mode and the intensity value. The LBF model has a good local adaptive performance, but overfitting may occur. The hybrid segmentation method based on the LBF and Chan–Vese models can better adapt to different image scenes while maintaining local adaptability and global consistency. In other words, the proposed method involves partitioning the image into multiple small regions, applying the LBF model for segmentation in each region, and leveraging the Chan–Vese model to enhance the overall consistency of segmentation results. In addition, this study incorporated E_{edge} to guide the separation of bony tissue, which is represented as $\int_{\Omega} g|\nabla H_{\varepsilon}(\varphi)|dy$.

$$\begin{cases} c_1 = \dfrac{\int_{\Omega} I(x)H_{\varepsilon}(\varphi)dx}{\int_{\Omega} H(\varphi)dx} \\[3mm] c_2 = \dfrac{\int_{\Omega} I(x)(1 - H_{\varepsilon}(\varphi))dx}{\int_{\Omega}(1 - H_{\varepsilon}(\varphi))dx} \end{cases} \tag{2}$$

$$\begin{cases} f_1 = \dfrac{K_{\sigma}(x) * (H_{\varepsilon}(\varphi) \cdot I(x))}{K_{\sigma}(x) * H_{\varepsilon}(\varphi)} \\[3mm] f_2 = \dfrac{K_{\sigma}(x) * ((1 - H_{\varepsilon}(\varphi)) \cdot I(x))}{K_{\sigma}(x) * (1 - H_{\varepsilon}(\varphi))} \end{cases}$$

where $I(y)$ represents the CBCT image, $H_{\varepsilon}(\varphi)$ is the normalised Heaviside function, δ_{ε} is the normalised Dirac function [25], λ_1, λ_2 are positive weights, K_{σ} denotes a Gaussian kernel of size σ, which is used to represent the small regions divided by the LBF model, the weight $\omega \in [0, 1]$ is expressed as the weight ratio of the two models, g is an edge indicator that is used to guide the global convex

segmentation and effectively find the edge of bony tissue. As shown in Equation (2), c_1 and c_2 represent the mean value of intensity inside and outside the level set curve, respectively, and the local average intensities f_1 and f_2 is interpreted as the weighted average of the intensity in the Gaussian window inside and outside the contour, respectively.

To minimise the energy function (1), the evolution equation of the level set can be obtained using variational and gradient descent methods. However, in the evolution of the level set model, a position with a positive value tends to $+\infty$, and a position with a negative value tends to $-\infty$; thus, the level set function cannot reach a stable state. Chan et al. [26] proposed a global optimal solution method in which the level-set function is restricted to the region [0,1] in each iteration, as shown in Equation (3).

$$\min_{0 \le u \le 1} \int_{\Omega} \left\{ \omega \cdot \left(\lambda_1 \cdot (I - c_1)^2 - \lambda_2 \cdot (I - c_2)^2 \right) + (1 - \omega) \cdot \left(\lambda_1 \cdot (I - f_1)^2 - \lambda_2 \cdot (I - f_2)^2 \right) \right\} \bullet u(x)\, dx + \int_{\Omega} g \cdot |\nabla u| dx \quad (3)$$

By setting $\Sigma = \{x : u(x) \ge \mu\}$, where $\mu \in [0, 1]$, the set Σ is obtained as the global segmentation results of a tooth. This problem can be solved based on the gradient descent and Eulerian–Lagrangian equations. However, this method occasionally results a slower regularisation process and higher time complexity. This study used the split Bregman method to solve unconstrained problems [27,28].

2.2. Curve segmentation lines for separating neighbouring teeth under severe dental crowding and tooth deformities

The direct segmentation of all teeth from CBCT images may result in boundary loss. Therefore, based on the assumption that a straight line can separate them, Xia et al. [29] proposed extracting an interdental straight segmentation line using the Radon transform to separate neighbouring teeth, and the method is represented by Equation (4); thus, each tooth is segmented independently:

$$R(\theta, \rho)(I(x, y)) = \int_{-\infty}^{+\infty} \int_{-\infty}^{+\infty} I(x, y) \delta(\rho - x\cos\theta - y\sin\theta) dx dy \quad (4)$$

However, impacted teeth or other structurally complex dental conditions can result in complex structural interferences between adjacent teeth, causing straight interdental segmentation lines that do not wholly and accurately separate neighbouring teeth. Fig. 2 (a), which simulates the close contact and relatively complex structure of two neighbouring teeth, shows that a significant segmentation error occurs when using an interdental straight segmentation line. Therefore, a method for separating neighbouring teeth based on a curved segmentation line is proposed. Keeping the θ value of the straight segmentation line unchanged, several straight lines with ρ in the range $[\rho - \alpha, \rho + \alpha]$ are selected (α is a positive integer), and the optimum point (minimum intensity value) is selected from the intersections at the common perpendicular of these $2\alpha + 1$ parallel lines. The optimum point is indicated by the red point. The curve formed by connecting the optimal points is expressed as the optimal interdental curve segmentation line of the neighbouring teeth, as shown in Fig. 2(b). This method detects optimal points between neighbouring deformed teeth and constructs a flexible and curved interdental segmentation line that can separate neighbouring adhesive teeth completely and accurately, and it has better generalisation than the traditional interdental straight segmentation line.

2.3. Independent tooth segmentation based on local level set model with adaptive edge feature enhancement

The geodesic active contour model is a level-set model based on the snake model and curve evolution theory [30]. It not only overcomes the limitation of the initial contour and free parameters in the solution process of the snake model but can also split or merge naturally in the evolution process to enable the detection of object boundaries. The LLIF model [36] assumes that local regions
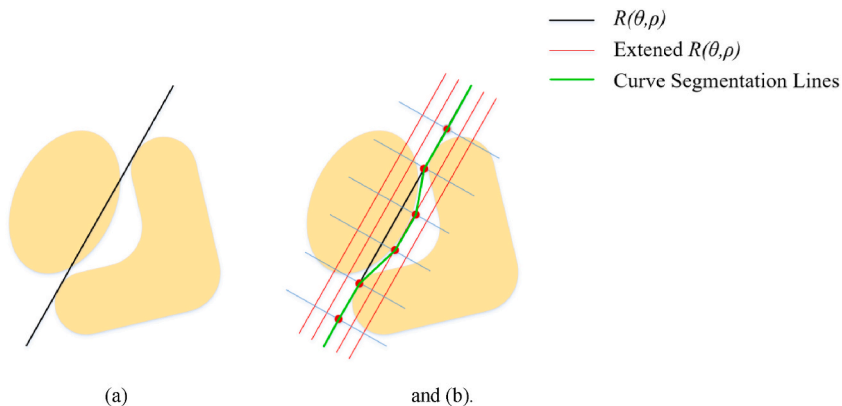
Fig. 2. (a) The two yellow regions represent neighbouring distorted teeth with complex structures, and the black lines represent the result of the straight-line segmentation extraction method. (b) The red straight line represents straight lines with the same angle as the original straight line, the blue straight line is perpendicular to the red straight line, and the optimal point is selected at the intersection of the red and blue lines, represented by the red points.

have spatially varying means and variances and follow a Gaussian distribution. It can accurately extract independent teeth when under image blurriness and intensity nonuniformity, which plays an important role in our research. In this study, the traditional geodesic active contour model was improved by enhancing the edge features for independent tooth segmentation and combined with the LLIF model [36], which is expressed as Equation (5):

$$E(\varphi) = \int_{\Omega} h_r \left| \nabla H(\varphi) \right| dx + \int_{\Omega} - \log p\left(I(x) \middle| U(x), S(x) \right) dx + \beta \int_{\Omega} (H(\varphi) - H(\varphi_0))^2 dx \tag{5}$$

$$\begin{cases} U(x) = u_1(x)H(\varphi) + u_2(x)(1 - H(\varphi)) \\ S(x) = s_1(x)H(\varphi) + s_2(x)(1 - H(\varphi)) \end{cases} \tag{6}$$

$$\begin{cases} u_1(x) = \dfrac{\int_{\Omega} K_L(y - x)I(y)H(\varphi)dy}{\int_{\Omega} K_L(y - x)H(\varphi)dy} \\ \\ u_2(x) = \dfrac{\int_{\Omega} K_L(y - x)I(y)(1 - H(\varphi))dy}{\int_{\Omega} K_L(y - x)(1 - H(\varphi))dy} \end{cases} \tag{7}$$

$$\begin{cases} s_1(x) = \dfrac{\int_{\Omega} K_L(y - x)(I(y) - U(x))^2 H(\varphi)dy}{\int_{\Omega} K_L(y - x)H(\varphi)dy} \\ \\ s_2(x) = \dfrac{\int_{\Omega} K_L(y - x)(I(y) - U(x))^2 (1 - H(\varphi))dy}{\int_{\Omega} K_L(y - x)(1 - H(\varphi))dy} \end{cases} \tag{8}$$

where h_r is the edge indicator used in this study, $\nabla H(\varphi)$ indicates the edge of the level set, $U(x)$ and $S(x)$ are represented in Equation (6), $u(x)$ and $s(x)$ are respectively represented by Equation (7) and Equation (8), K_L is a Gaussian window, and the actual tooth boundary was found by minimising the energy function.

2.3.1. Selecting the key region for independent tooth

In this study, the influence of unnecessary factors on the image was eliminated as much as possible. Based on the theory that the contours of the prior layers of the same tooth are similar, the region close to the boundary of the prior contour of the tooth was defined as the key region, and the region far away from the boundary was defined as the non-key region. In this experiment, the calculations were limited to the key region, thereby minimising the impact of extraneous gradients on the segmentation of individual teeth and mitigating the effects of scattering caused by the root canal treatment The key region of an independent tooth image is defined as follows: Let the value in the contour region of the prior independent tooth be p (yellow region in Fig. 3(a)), and the value outside the contour region of the tooth be 0 (white region in Fig. 3(a)). A $k * k$ scale filter is applied to the results of the tooth before the contour labels to determine the key region. The obtained region $R_T = \{x : 1 < I(x) < p\}$ is the key region in the edge indicator, and regions $C = \{x : I(x) = p\}$ and $D = \{x : I(x) = 0\}$ are the internal and external non-key regions, respectively (Fig. 3(b)). In this study, the R_T key region was defined as the active region of the edge indicator.

2.3.2. Local intensity fitting coefficient for adaptive enhancement

Because the root intensity is similar to that of the surrounding bony tissue, the gradient between the root and surrounding alveolar bone is not prominent, which results in an insufficient constraint on the edge indicator for actual tooth boundaries. Researchers have attempted to use hybrid level-set models to address this problem. A general hybrid level set model is primarily driven by the intensity energy and edge detection energy of an image, and this method is only effective for roots that are not in close contact with the alveolar
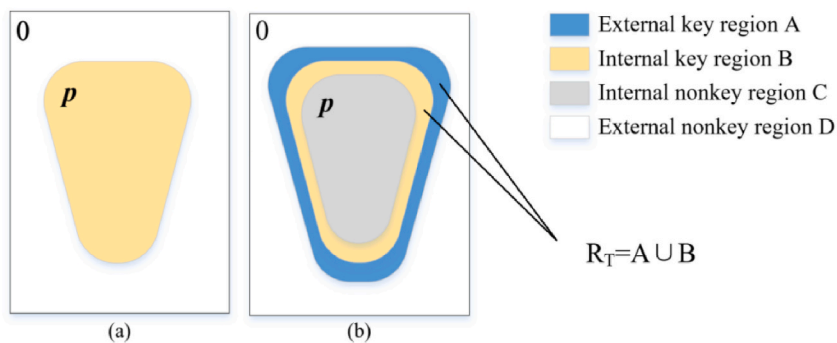
Fig. 3. (a) Prior contour region of a tooth. The yellow region indicates the prior contour region, and the white region indicates the region outside the prior contour region. (b) The result of a filter operation on the labels of the prior contour region of the tooth. The blue and yellow regions represent the key region R_T, the blue region A is the external key region, and the yellow region B is the internal key region. Regions C and D are considered non-key regions because they are too far away from the prior contour curve.

bone; otherwise, the actual tooth boundary feature is not prominent, and the teeth and alveolar bone have similar image intensities. Thus, the intensity and edge energy terms in the hybrid level set cannot effectively detect the boundary at the root and may cause severe boundary leakage. However, in clinical dentistry, tooth rotation or displacement caused by dental crowding often results in excessive contact between the teeth roots and the alveolar bone, resulting in the loss of their boundaries in CBCT images and significantly affecting the segmentation process. Inaccurate differentiation of the two causes the reconstructed root to not be enveloped by the alveolar bone, resulting in deviations in doctors' judgments of the shape of the alveolar bone and the anatomical position relationship with the root, thereby increasing the corresponding risk of orthodontic treatment. To address this problem, the local intensity fitting coefficient is proposed to enhance the weight of the feature between the roots and alveolar bone in the key region, and the local intensity fitting coefficient is defined as Equation (9):

$$L_c(x) = \begin{cases} \tau \cdot tanh(-w \cdot FI(x)) + \tau + 1 & x \in R_T \\ 0 & x \notin R_T \end{cases} \tag{9}$$

$$FI(x) = \mu_t(x) - [\mu_b(x) + \sigma_b(x)] \tag{10}$$

where τ is the positive integer weight, and w is the coefficient that affects the degree of bending of the hyperbolic tangent function $tanh(x)$. $FI(x)$ is represented by Equation (10), which is used to quantify the degree of intensity difference between teeth and alveolar bone. $\mu_t(x), \mu_b(x)$, and $\sigma_b(x)$ are the mean value of the tooth intensity, mean value of the alveolar bone intensity, and variance of the alveolar bone intensity in a small region with the central point x, respectively, and R_T is the key region in the image.

Consider a case in which the tooth is in close contact with the alveolar bone. The minor intensity difference inside and outside the contour in a small region on the boundary of the tooth causes the local intensity fitting coefficient to increase, increasing the weight of the gradient at position x and reducing the evolution speed of the level-set curve. When the tooth and alveolar bone are not in close contact, the small region centred on a point x have a significant intensity difference inside and outside the tooth contour, making the local intensity fitting coefficient $L_c(x) \approx 1$. This coefficient adjusts the weight of the edge indicator at the tooth boundary based on the different edge features. Experiments have shown that this coefficient can effectively distinguish between the root and alveolar bone in close contact caused by tooth rotation and displacement. It prevents edge leakage and improves segmentation accuracy in clinical dentistry.

2.3.3. Boundary confidence coefficient for detecting tooth boundary accurately

Owing to the high tooth shape similarity between adjacent slices in CBCT images, researchers have introduced a tooth shape prior to the constraint term in the level set to make the tooth shape segmented from the current layer as similar as possible to that in the previous layer [5,19,21]. The segmentation results obtained by introducing tooth shape prior constraints not only make the reconstructed 3D dental model smoother but also prevent boundary leakage errors to a certain extent. Specifically, the traditional tooth shape prior constraint is primarily constrained by continuously superimposing the signed distance of the tooth shape before the curve evolution process. Although this constraint can make the level-set curve as similar as possible to the prior curve, it does not contribute to determining the actual tooth boundary. Therefore, a boundary confidence coefficient is proposed to constrain the edge indicator. This can prevent the level-set curve from evolving too far from the prior and guides the evolution of the level-set curve. The boundary confidence coefficient is defined as Equation (11)

$$B_c(x) = \begin{cases} (1 - \text{Norm}(|\varphi_0|))^\kappa & \varphi \in R_T \\ 0 & \varphi \notin R_T \end{cases} \tag{11}$$

$\text{Norm}(\cdot)$ is the normalization function defined as Equation (12)

$$\text{Norm}(|\varphi_0|) = \frac{|\varphi_0| - min(|\varphi_0|)}{max(|\varphi_0|) - min(|\varphi_0|)} \tag{12}$$

The tooth shape prior φ_0 is standardised using $\text{Norm}(\cdot)$. The coefficient optimises the edge indicator according to the distance between the evolving curve and the prior contour of a tooth and selects a more precise tooth boundary in the case of a tooth in close contact with the alveolar bone.

Furthermore, although the local intensity fitting coefficient effectively prevents the level-set curve from spreading to the alveolar bone around the tooth when the centre point x is far from the tooth boundary, the results from the local intensity fitting coefficient used to increase the weight of the gradient at this point are unreliable. Therefore, the boundary confidence coefficient can also constrain the local intensity fitting coefficient to detect precise tooth boundaries in cases of tooth rotation and displacement.

2.3.4. Construction of the multiscale edge indicator with adaptive edge feature enhancement

Image gradient information is essential in tooth segmentation and has been widely used in level-set models [5,18–23]. The traditional edge indicator constructed using the image gradient was used to control the speed of curve evolution. The robustness of the traditional edge indicator worsens if a small Gaussian kernel is used to process dental CBCT images while smoothing them. The edge indicator may be unable to accurately segment an image with inhomogeneous intensity if a large Gaussian kernel is used [31]. Thus, utilizing a multiscale Gaussian kernel and gradient direction is indispensable to determining and retaining the effective gradient.

The image intensity is also an important piece of information for tooth segmentation. Without considering the internal contours caused by the pulp cavity, the tooth region has higher intensity. In this study, the gradient information was taken as the primary

premise for edge determination, and the tooth boundary was determined by influencing the gradient weight under different image intensities. In this study, the weight of the gradient increased with the image intensity because the image intensity of the tooth was generally more prominent than that of the other tissues.

The objective of the edge indicator is to remove the influence of noise while preserving the edge information and ensuring that the contour curve stops at the target boundary. Because the root boundaries are blurred, the gradient at the boundary is not prominent, and an edge indicator function with a rapid decline should be adopted for an image with a slight edge gradient value [32,33]. This study adopted a steep-edge indicator by combining multiscale gradient and intensity information as Equation (13).

$$
h_r(x) = \begin{cases} \rho \cdot \exp \left\{ \dfrac{-\left| \dfrac{1}{K} \displaystyle\sum_{S=1}^{K} \nu \cdot [\nabla G_s \cdot I(x)]^3 \cdot I_w(x) \cdot L_c(x) \cdot B_c(x) \right|}{2\sigma^2} \right\} & \begin{array}{l} \nabla I_G \cdot \nabla \varphi_g \geq 0 \\ \nabla I_G \cdot \nabla \varphi_g < 0 \end{array} \\ 1 \end{cases} \tag{13}
$$

where $\nabla G_s \cdot I(x)$ is the gradient of image $I(x)$ smoothed by a Gaussian filter of scale $(2S+1)*(2S+1)$, ν is the positive weight, $\nabla \varphi_g$ is the direction gradient of the level set evolution, σ is the variance of the Gaussian kernel, ρ is the weight coefficient, $I_w(x)$ represents the weight of the image intensity, and $L_c(x)$ and $B_c(x)$ are the coefficients to optimise the edge indicator.

2.3.5. Evolution of level set curves

The minimisation of functional energy (5) was solved using an explicit iteration scheme based on the following gradient descent flows as Equation (14):

$$
\frac{\partial \varphi}{\partial t} = \delta(\varphi) div \left(h_r \bullet \frac{\nabla \varphi}{|\nabla \varphi|} \right) + \delta(\varphi) \left[-(s_1 - s_2) + 2(I - U)(u_1 - u_2) + \frac{(I - U)^2(s_1 - s_2)}{S_j} \right] - 2\beta \delta(\varphi)(H(\varphi) - H(\varphi_0)) \tag{14}
$$

where t is the iteration time, $t > 0$, and *div* is the divergence operator.

In addition, the level-set function was regularised by convolving it with a Gaussian filter. This regularisation method based on a Gaussian filter can effectively prevent the level set from being too steep or flat and has a higher efficiency [34].

2.4. Performance evaluation

All methods applied in this study were implemented on a *Windows 10* operating system with an Intel I9-10900 KF with a 5.3 GHz CPU and 64 GB RAM. According to experience, the parameters $\lambda_1 = 1, \lambda_2 = 1, \mu = 0.6$ were set in the global convex segmentation process. The parameter α was set to 2 in the extraction of interdental curve segmentation lines, which means that the curve was constructed from five straight lines. The following parameters were set in the independent segmentation of the local level set: $\nu = 1$, $K = 3, \tau = 4, \kappa = 4$.

The experiments were evaluated by comparing the segmentation results obtained in this study with those obtained using manual segmentation performed by multiple professional clinicians. Five metrics were used: volume difference (VD, mm^3), Dice similarity coefficient (DSC, %), average symmetric surface distance (ASSD, mm), maximum symmetric surface distance (MSSD, mm), and distance of tooth centroids (DTC, mm) [31], which are defined as follows:

$$
VD = |V_R - V_A| \tag{15}
$$

$$
DSC = \frac{2V_R \cap V_A}{V_R + V_A} \tag{16}
$$

V_R and V_A in *VD* and *DSC* indices represent the volume under the gold standard and the volume segmented by the algorithm, respectively.

$$
ASSD(S_R, S_A) = mean\{mean\{dist(a, S_R), a \in S_A\}, mean\{dist(r, S_A), r \in S_R\}\} \tag{17}
$$

$$
MSSD(S_R, S_A) = max\{max\{dist(a, S_R), a \in S_A\}, max\{dist(r, S_A), r \in S_R\}\} \tag{18}
$$

S_R and S_A in *ASSD* and *MSSD* denote the surfaces partitioned under the gold standard and algorithm, respectively. $dist(x, S)$ denotes the shortest Euclidean distance from point x to plane S, and $mean\{\bullet\}$ denotes the arithmetic mean operator.

$$
DTC = \frac{1}{L} \sum_{i=1}^{L} d(S_i(R), S_i(A)) \tag{19}
$$

$d(S_i(A), S_i(B))$ is the shortest Euclidean distance between the centroids under the gold standard and algorithm.

3. Results

3.1. Qualitative results

The proposed method was compared with two high-performance level set models and one method that combines deep learning. Gan's method [5] is a hybrid level set model that includes local intensity energy, global intensity energy, edge detection energy, and shape constraint energy. Gan's method [21] introduces intensity information into the edge detector and optimises the shape constraint term. Xie's method [35] combines deep learning and level-set methods and constrains the evolution of level-set curves through ellipse priors.

As shown in Fig. 4, Gan's method [5] had a significant under-segmentation at the tooth root under tooth rotation caused by adhesion between the tooth root and alveolar bone. The multiscale image gradient information used in this study can be effectively obtained at different scales to maintain the actual gradient. In addition, the boundary confidence coefficient was weighted according to the distance from the level-set curve to the prior. This solves the problem in which the traditional prior energy term coefficient is difficult to control and makes it easier for the level-set curve to stop at the actual boundary of the tooth.

Gan et al. [21] introduced intensity information to distinguish teeth from alveolar bone. However, for malocclusions, such as tooth rotation and displacement, the roots and alveolar bone often have close contact and similar image intensity, which results in edge leakage and causes a risk that the alveolar bone may not surround the root in the 3D dental model and may cause tooth loss after orthodontic treatment. The local intensity fitting coefficient can enhance the feature weight at the tooth boundary according to the similarity of the tooth and alveolar bone intensities and perform an edge-based distance constraint through the boundary confidence coefficient. Fig. 5 shows that the method proposed in this paper can accurately distinguish the close contact between the root and alveolar bone caused by tooth rotation and displacement and achieve similar results to manual segmentation.

Xie's method can accurately and effectively split teeth [35]. However, at the location of severe dental crowding or large splitting of the tooth root, this can result in inaccurate ellipse prior detection, resulting in an error in the segmentation result, as shown in Fig. 6. The proposed interdental curve segmentation lines can ensure independence between teeth in the process of tooth segmentation and can effectively separate neighbouring teeth under complex structural interference. In addition, Xie's method occasionally cannot distinguish between closely touched teeth and alveolar bones. This paper proposes two coefficients that can optimise the edge indicator and obtain satisfactory segmentation results. Fig. 7 shows that the segmentation results without using the two optimised coefficients had an apparent boundary leakage error caused by the close contact between the tooth and alveolar bone. The segmentation results obtained using the two optimised coefficients were similar to the manual segmentation results.

The proposed method accurately separates and segments neighbouring teeth even in the presence of complex structural interferences. It also achieves stable and precise tooth segmentation under conditions of tooth rotation and displacement caused by dental crowding and enables the reconstruction of a stable 3D dental model. Fig. 8 shows the precise segmentation of both the upper and lower jaw teeth using the proposed method. Even in cases of complex structural interference between the impacted teeth and their adjacent teeth, this method consistently distinguishes between them and achieves high-precision tooth segmentation. Fig. 9 shows the segmentation results for tooth rotation and displacement caused by dental crowding.
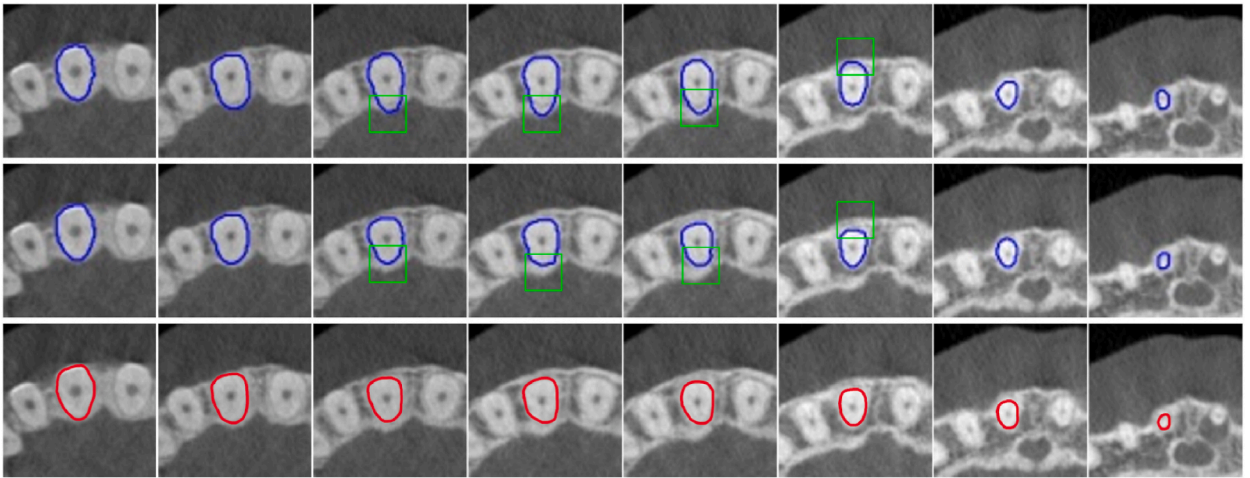
3.2. Quantitative results

In this study, the performance of the proposed method was compared with that of three other methods in terms of five metrics.
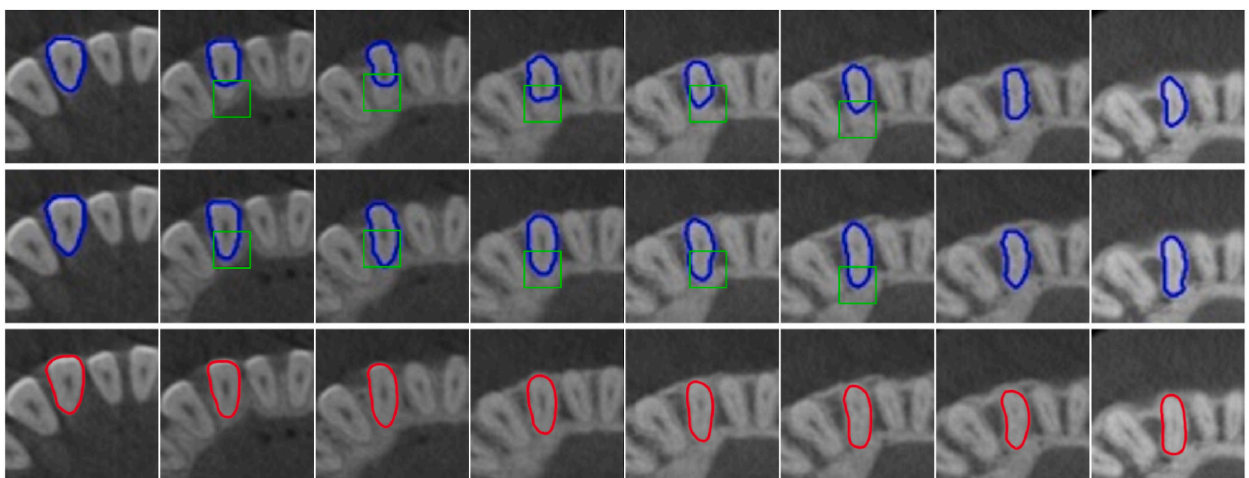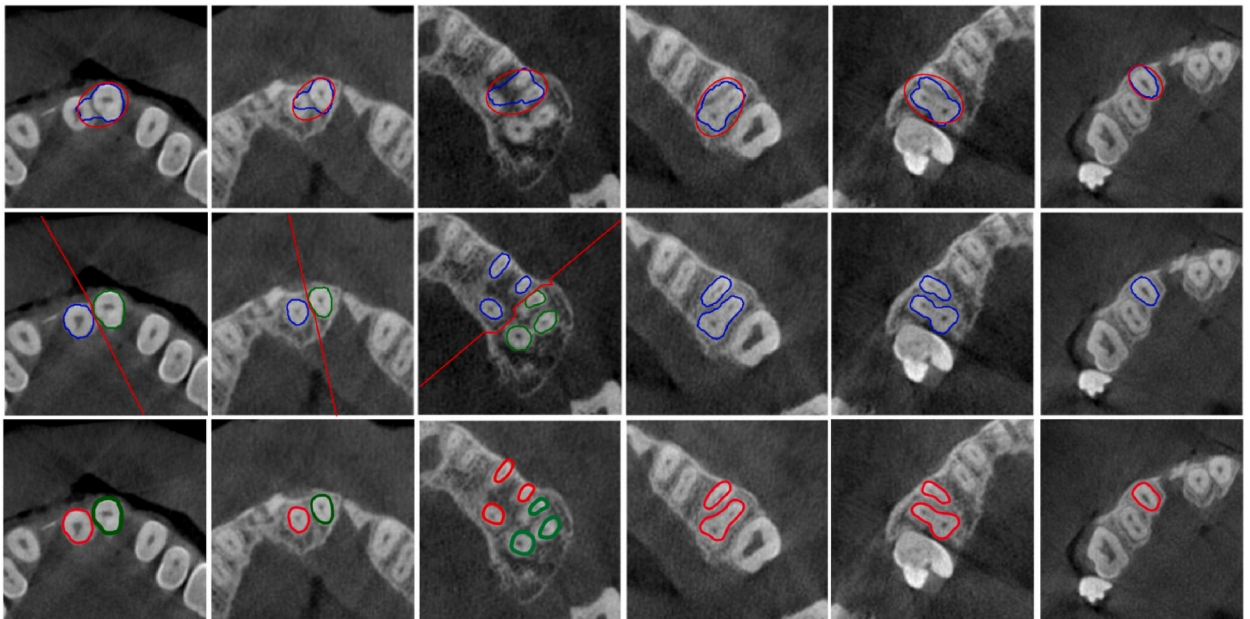

Fig. 4. The first to third rows represent the segmentation results of Gan et al. [5], the segmentation results of the proposed method, and the result of manual segmentation.

Fig. 5. The first to third rows represent the segmentation results of Gan et al. [21], the proposed method results, and the result of manual segmentation.


Fig. 6. The first to third rows represent the segmentation results of Xie et al. [35], where the ellipse in the figure represents a prior ellipse for tooth segmentation, the segmentation results of the proposed method, where the curve in the figure represents the curve segmentation lines between neighbouring teeth, and the result of manual segmentation, respectively.

Fig. 10 shows the quantitative results of Gan et al. [5], Gan et al. [21], Xie et al. [35], and the proposed method for the four types of teeth. The results showed that the segmentation performance of the proposed method was better than that of Gan's [5] method for four types of teeth. Compared with the segmentation results of Gan et al. [21], the proposed method achieved significantly better segmentation results for the incisors, canines, and premolars. Xie's method [35] achieved satisfactory results for canine teeth. However, for complex structural interference between adjacent teeth, the prior elliptical detection is not always accurate in the position of close contact of the incisors or furcated molars, which leads to a decrease in accuracy and a more significant standard deviation. Although not significantly advantageous under the indicators of volume differences and the Dice similarity coefficient, the results of the method used in this study have significant advantages in terms of the distance between tooth centroids. Compared with the other methods, the values of the DTC indicators for the four types of teeth were reduced, which indicated that the results of the proposed method had more minor deviations in terms of tooth orientation and strong stability. Owing to the importance of tooth orientation in reflecting anatomical information, the proposed method has clinical significance [5,21,35]. Table 1 presents detailed data for the quantitative segmentation accuracy of teeth using the presented method. Table 2 and Table 3 respectively provide detailed data for the quantitative
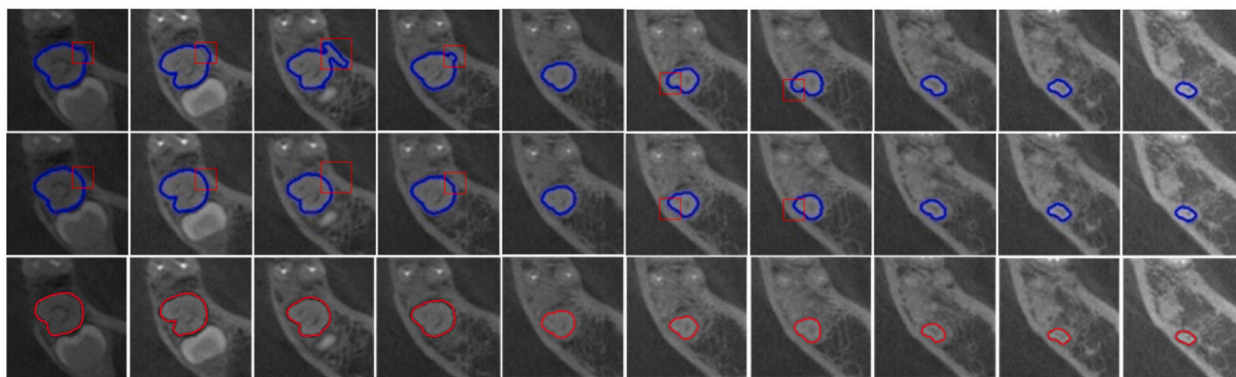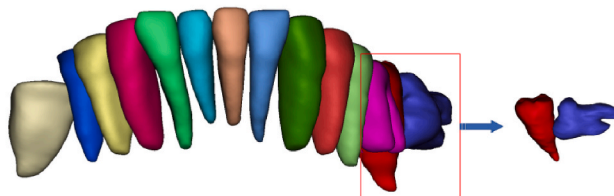
Fig. 7. Comparison of segmentation results with and without two optimization coefficients in the edge indicator. The first row shows the segmentation results without using two optimization coefficients, and the second row shows the results using two optimization coefficients. The third row shows the manual segmentation.
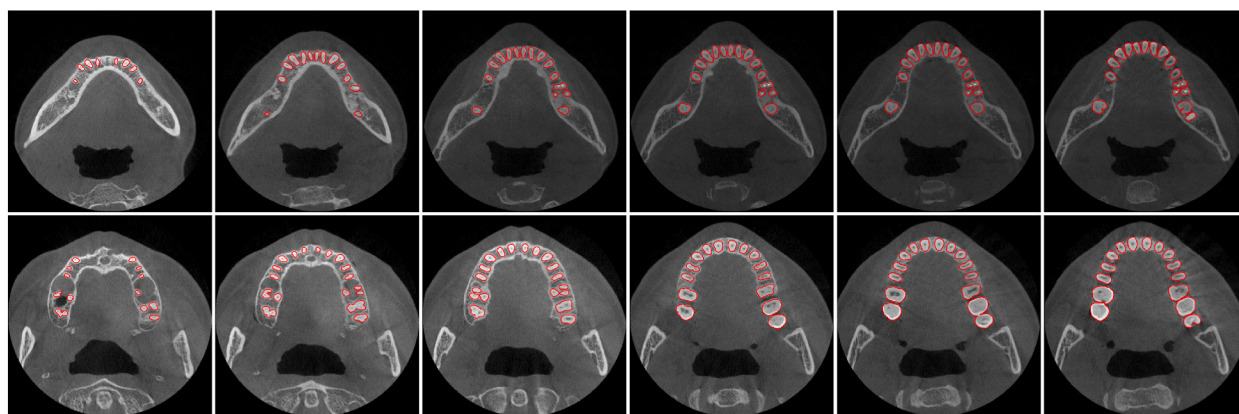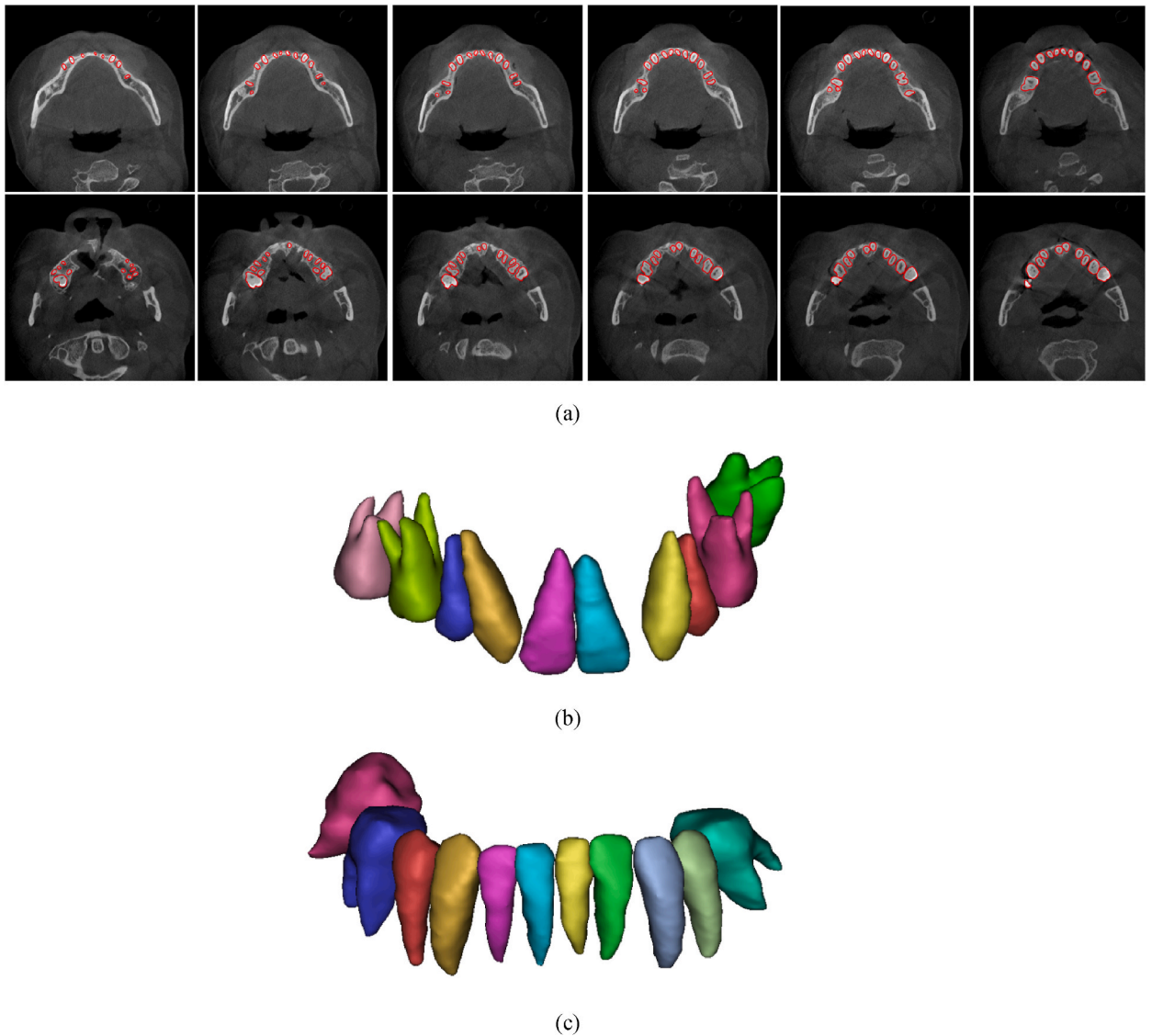

(a)
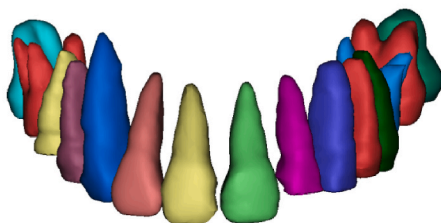
(b)

(c)

Fig. 8. (a) Results of tooth segmentation (maxillary slices and mandible slices), (b) 3D dental model reconstruction of the upper jaw, and (c) 3D dental model reconstruction of the lower jaw, characterized by complex structural interferences between impacted teeth and their adjacent teeth.

(a)

(b)

(c)

Fig. 9. (a) Results of tooth segmentation under malocclusion (maxillary slices and mandible slices), and (b) 3D dental model reconstruction of the upper jaw, featuring tooth rotation and displacement caused by dental crowding, and (c) 3D dental model reconstruction of the lower jaw, featuring tooth rotation and displacement caused by mild dental crowding.

segmentation accuracy of upper jaw teeth and lower jaw teeth using the presented method. ($p < 0.05$, *t*-test).

4. Discussion

Complete 3D dental information is essential for orthodontic diagnosis and treatment planning in digital and quasi-medical medicine. CBCT is the only source of root data and segmenting teeth using CBCT is an essential step in constructing a complete 3D dental model. Although many studies have been conducted on tooth segmentation, research on tooth segmentation in complex oral conditions, such as complex structural interference between adjacent teeth or tooth rotation and displacement caused by dental crowding, is rare. However, patients requiring CBCT imaging often experience dental problems. In response to these challenges, the proposed method can accurately separate neighbouring teeth with complex structural interference, providing doctors with more accurate data on tooth boundary structures in clinical orthodontics, and is more robust than other methods. Patients' teeth typically undergo crowding, which can potentially result in tooth rotation and displacement, resulting in close contact between the root and alveolar bone. However, existing methods often cannot accurately distinguish between the root and the alveolar bone, resulting in the reconstructed root not being enveloped by the alveolar bone. In orthodontic treatment, the alveolar bone should be reconstructed and reshaped based on plasticity to achieve tooth correction. The proposed method can accurately distinguish the close contact between
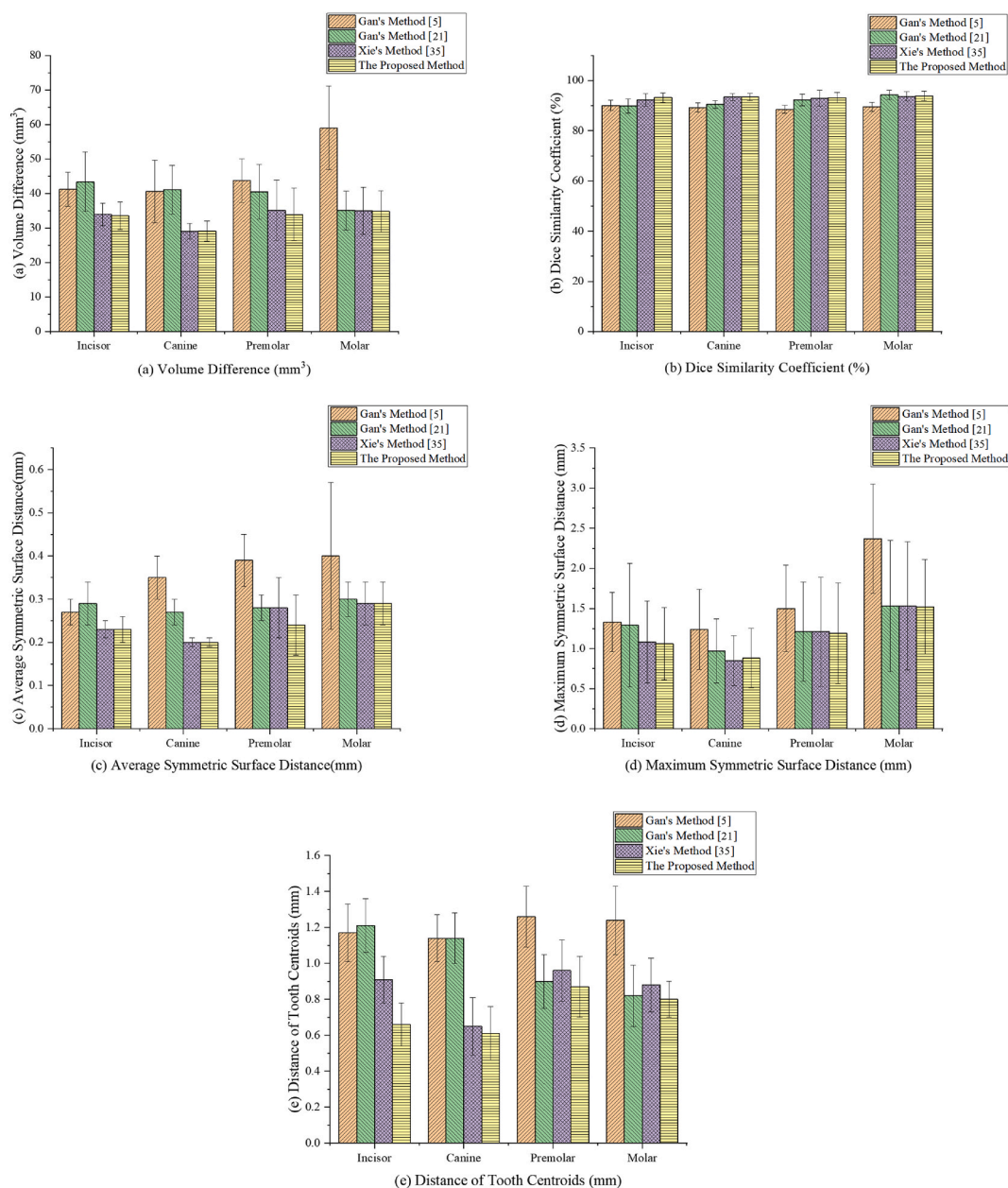
Fig. 10. Quantitative comparison of segmentation accuracy, (a) volume difference, (b) Dice similarity coefficient, (c) average symmetric surface distance, (d) maximum symmetric surface distance, and (e) distance of tooth centroids.

the root and alveolar bone caused by tooth rotation and displacement and ensure that the reconstructed root is not exposed.

First, global convex segmentation was used to segment the bony tissue in the CBCT images to reduce the influence of soft tissue and air on segmentation.

Second, the primary objective of this step was to separate the neighbouring teeth accurately. Xia et al. proposed extracting the interdental straight segmentation lines of neighbouring teeth using Radon transform [29]. However, this method cannot accurately separate two adhered teeth with complex structural interference. Dental problems are commonly encountered in clinical practice. The advantage of the proposed method is that it extends the straight interdental segmentation line to select appropriate segmentation points. The interdental curve segmentation line connected by these points has flexible and versatile characteristics and can more accurately separate neighbouring teeth under complex structural interference.

Third, local-level sets were used to separate individual teeth. Because the segmentation results are affected by noise in the CBCT images, a Gaussian filter is used to smooth the images to effectively address noise and inhomogeneous intensity. However, it is difficult to determine the Gaussian filter scale. In this experiment, the multiscale Gaussian filter effectively obtained the gradient information of

Table 1
Quantitative segmentation accuracy of the presented method.

Teeth ($p < 0.05$, t-test)	Approach	VD (mm^3)	DSC (%)	ASSD (mm)	MSSD (mm)	DTC (mm)
Incisor	Gan's method [5]	41.27 ± 4.95	90.11 ± 2.10	0.27 ± 0.03	1.33 ± 0.37	1.17 ± 0.16
	Gan's method [21]	43.41 ± 8.66	89.89 ± 2.83	0.29 ± 0.05	1.29 ± 0.77	1.21 ± 0.15
	Xie's method [35]	33.93 ± 3.20	92.27 ± 2.47	**0.23 ± 0.02**	1.08 ± 0.51	0.91 ± 0.13
	Proposed method	**33.57 ± 4.04**	**92.30 ± 1.90**	0.23 ± 0.03	**1.06 ± 0.45**	**0.66 ± 0.12**
Canine	Gan's method [5]	40.61 ± 9.03	89.27 ± 1.87	0.35 ± 0.05	1.24 ± 0.50	1.14 ± 0.13
	Gan's method [21]	41.13 ± 7.03	90.49 ± 1.56	0.27 ± 0.03	0.97 ± 0.40	1.14 ± 0.14
	Xie's method [35]	**29.05 ± 2.24**	93.45 ± 1.33	0.20 ± 0.01	**0.85 ± 0.31**	0.65 ± 0.16
	Proposed method	29.09 ± 2.92	**93.47 ± 1.42**	0.20 ± 0.01	0.88 ± 0.37	**0.61 ± 0.15**
Premolar	Gan's method [5]	43.75 ± 6.26	88.59 ± 1.53	0.39 ± 0.06	1.50 ± 0.54	1.26 ± 0.17
	Gan's method [21]	40.51 ± 7.98	92.29 ± 2.24	0.28 ± 0.03	1.21 ± 0.62	0.90 ± 0.15
	Xie's method [35]	35.10 ± 8.79	93.01 ± 3.14	0.28 ± 0.07	1.21 ± 0.68	0.96 ± 0.17
	Proposed method	**33.89 ± 7.62**	**93.24 ± 2.11**	**0.24 ± 0.07**	**1.19 ± 0.63**	**0.87 ± 0.17**
Molar	Gan's method [5]	59.03 ± 12.16	89.60 ± 1.84	0.40 ± 0.17	2.37 ± 0.68	1.24 ± 0.19
	Gan's method [21]	35.07 ± 5.62	**94.37 ± 1.79**	0.30 ± 0.04	1.53 ± 0.82	0.82 ± 0.17
	Xie's method [35]	35.04 ± 6.80	93.72 ± 1.87	0.29 ± 0.05	1.53 ± 0.80	0.88 ± 0.15
	Proposed method	**34.83 ± 6.01**	93.89 ± 1.85	**0.29 ± 0.05**	l.52 ± 0.59	**0.80 ± 0.10**

Table 2
Quantitative segmentation accuracy of upper jaw teeth.

Upper jaw teeth ($p < 0.05$, t-test)	Approach	VD (mm^3)	DSC (%)	ASSD (mm)	MSSD (mm)	DTC (mm)
Incisor	Gan's method [5]	41.14 ± 4.87	90.35 ± 1.95	0.26 ± 0.03	1.28 ± 0.35	1.15 ± 0.17
	Gan's method [21]	42.85 ± 8.01	90.02 ± 2.78	0.29 ± 0.05	1.28 ± 0.71	1.20 ± 0.16
	Xie's method [35]	33.80 ± 3.12	92.39 ± 2.57	**0.22 ± 0.02**	1.07 ± 0.53	0.90 ± 0.13
	Proposed method	**33.53 ± 4.10**	**92.51 ± 1.93**	0.22 ± 0.03	**1.05 ± 0.45**	**0.65 ± 0.11**
Canine	Gan's method [5]	39.50 ± 9.06	89.40 ± 1.80	0.33 ± 0.05	1.22 ± 0.49	1.13 ± 0.14
	Gan's method [21]	40.70 ± 7.08	90.53 ± 1.48	0.26 ± 0.03	0.96 ± 0.43	1.13 ± 0.14
	Xie's method [35]	**28.86 ± 2.37**	93.50 ± 1.39	0.20 ± 0.01	**0.84 ± 0.33**	0.64 ± 0.15
	Proposed method	29.02 ± 3.13	**93.51 ± 1.51**	**0.20 ± 0.01**	0.86 ± 0.34	**0.60 ± 0.14**
Premolar	Gan's method [5]	43.49 ± 6.15	88.63 ± 1.50	0.38 ± 0.05	1.48 ± 0.53	1.24 ± 0.19
	Gan's method [21]	40.61 ± 8.32	92.34 ± 2.32	0.27 ± 0.03	1.18 ± 0.62	0.88 ± 0.12
	Xie's method [35]	35.69 ± 8.27	93.09 ± 3.29	0.27 ± 0.08	1.19 ± 0.67	0.95 ± 0.16
	Proposed method	**33.78 ± 7.46**	**93.30 ± 1.79**	**0.23 ± 0.08**	**1.16 ± 0.64**	**0.86 ± 0.16**
Molar	Gan's method [5]	58.34 ± 12.21	89.67 ± 1.87	0.39 ± 0.17	2.31 ± 0.64	1.24 ± 0.18
	Gan's method [21]	34.81 ± 5.89	**94.57 ± 1.73**	0.30 ± 0.04	1.52 ± 0.79	0.81 ± 0.15
	Xie's method [35]	34.81 ± 6.71	93.82 ± 1.90	0.29 ± 0.05	1.52 ± 0.78	0.86 ± 0.16
	Proposed method	**34.36 ± 6.19**	93.95 ± 1.84	**0.29 ± 0.04**	**1.52 ± 0.61**	**0.80 ± 0.11**

Table 3
Quantitative segmentation accuracy of lower jaw teeth.

Lower jaw teeth ($p < 0.05$, t-test)	Approach	VD (mm^3)	DSC (%)	ASSD (mm)	MSSD (mm)	DTC (mm)
Incisor	Gan's method [5]	41.47 ± 5.08	89.93 ± 2.29	0.28 ± 0.03	1.36 ± 0.38	1.18 ± 0.16
	Gan's method [21]	43.69 ± 9.12	89.81 ± 2.85	0.29 ± 0.04	1.31 ± 0.83	1.22 ± 0.15
	Xie's method [35]	34.06 ± 3.29	92.08 ± 2.38	0.23 ± 0.03	1.10 ± 0.49	0.91 ± 0.12
	Proposed method	**33.64 ± 4.26**	**92.19 ± 1.79**	**0.23 ± 0.03**	**1.08 ± 0.44**	**0.67 ± 0.12**
Canine	Gan's method [5]	41.85 ± 9.38	89.14 ± 1.92	0.36 ± 0.04	1.26 ± 0.51	1.14 ± 0.13
	Gan's method [21]	41.40 ± 6.91	90.44 ± 1.61	0.27 ± 0.03	0.99 ± 0.36	1.15 ± 0.13
	Xie's method [35]	**29.18 ± 2.20**	**93.39 ± 1.28**	0.20 ± 0.01	**0.85 ± 0.30**	0.65 ± 0.16
	Proposed method	29.18 ± 2.80	93.39 ± 1.37	**0.20 ± 0.01**	0.90 ± 0.40	**0.61 ± 0.16**
Premolar	Gan's method [5]	43.94 ± 5.64	88.54 ± 1.55	0.39 ± 0.07	1.51 ± 0.56	1.27 ± 0.16
	Gan's method [21]	40.37 ± 7.52	92.25 ± 2.18	0.28 ± 0.03	1.26 ± 0.61	0.91 ± 0.17
	Xie's method [35]	34.76 ± 9.25	92.97 ± 2.98	0.29 ± 0.07	1.23 ± 0.69	0.97 ± 0.17
	Proposed method	**33.95 ± 7.81**	**93.17 ± 2.58**	**0.25 ± 0.06**	1.23 ± 0.63	**0.88 ± 0.17**
Molar	Gan's method [5]	59.67 ± 11.95	89.54 ± 1.81	0.41 ± 0.16	2.43 ± 0.71	1.24 ± 0.19
	Gan's method [21]	35.46 ± 5.49	**94.22 ± 1.81**	0.31 ± 0.04	1.54 ± 0.84	0.83 ± 0.20
	Xie's method [35]	35.32 ± 6.95	93.64 ± 1.81	0.29 ± 0.05	1.54 ± 0.81	0.90 ± 0.14
	Proposed method	35.41 ± 5.83	93.84 ± 1.86	**0.29 ± 0.05**	**1.53 ± 0.57**	**0.81 ± 0.10**

an image at different scales to maintain the actual gradient. However, the tooth boundaries in CBCT images were blurred, making it difficult to segment individual teeth. Gan et al. developed a hybrid level-set model to extract accurate tooth contours [5]. Wang et al. proposed a new method that uses a variational level-set formulation to accurately segment tooth roots [31]. This novel hybrid level set model is composed of a local LLIF energy term, a shape prior constraint energy term with adaptive weights, and an RD regularisation

energy term, which the LLIF energy term aids in overcoming edge blurring and inhomogeneous intensity. The RD energy term is used to effectively regulate the level set evolution. Although these methods can overcome the problems of blurred edges and inhomogeneous intensity to some extent, they cannot effectively distinguish teeth with similar intensities from the alveolar bone. Gan et al. introduced image intensity information as an edge indicator [21]. Based on the theory that the image intensity of the tooth is slightly higher than that of the surrounding bony tissue, a geodesic active contour model with a shape prior constraint is guided by an edge indicator to distinguish the root from the adjacent alveolar bone. However, the image intensities of the two are very similar when they are in close contact, and Gan's method is still impractical for distinguishing them. However, in clinical dentistry, tooth alignment often involves rotation and displacement, resulting in close contact between the root and alveolar bone. Using previous methods to segment teeth may not accurately detect both, resulting in the reconstructed root not being enveloped by the alveolar bone, thus increasing the risk of orthodontic treatment. Therefore, the two optimization factors proposed in this paper can enhance the feature weight at the tooth boundary, apply edge constraints, and more effectively distinguish teeth with similar image intensities and close contact with the alveolar bone.

In addition, Xie et al. proposed an automatic tooth segmentation model combining deep learning and level-set methods [35], using the deep learning method to detect the position and size of each tooth and generate an ellipse from the detected boundary box as a priori. This method adapts better to the tooth shape and reduces the accumulated error to a certain extent. However, elliptical priors exhibit poor adaptability to teeth with complex structures. In clinical practice, teeth often exhibit complex oral conditions resulting in errors in elliptical priors and inaccurate segmentation results. This causes a significant deviation in the tooth direction; therefore, the segmentation accuracy under the DTC indicator was unsatisfactory. In this study, interdental curve segmentation lines were constructed to separate neighbouring teeth under complex structural interference before independent tooth segmentation. This can eliminate segmentation errors caused by inaccurate elliptical priors and avoid detecting the roots of different teeth in the same tooth. In addition, teeth in close contact with the alveolar bone are not easily distinguishable using Xie's method. Therefore, the two optimization factors proposed in this study can guide the level-set curve to easily evolve to the actual boundary of the tooth, effectively control the deviation of the tooth direction, and achieve significant advantages under DTC indicators.

Accurate tooth segmentation from CBCT images is essential in building a complete 3D dental model. This can assist dentists in understanding the shape and structure of teeth and improve treatment efficiency, which is vital in clinical practice. Accurate tooth segmentation under conditions of complex structural interference between adjacent teeth or tooth rotation and displacement caused by dental crowding can be achieved by applying this solution, and the segmentation results can be used to reconstruct a high-precision and complete 3D dental model.

Finally, our study had some limitations. We focused exclusively on tooth segmentation in dental CT images acquired from subjects' teeth in the open-bite position. Notably, the proposed method may not accurately segment images containing metallic artefacts. These complex scenarios can also provide directions for future research.

5. Conclusion

This study developed a method for accurate tooth segmentation from CBCT images of complex oral conditions, such as complex structural interference between adjacent teeth, tooth rotation, and displacement caused by dental crowding. First, global convex segmentation was performed on each CBCT image. Thereafter, a method for constructing flexible and curved segmentation lines between neighbouring teeth that can accurately detect neighbouring teeth boundaries, even in scenarios characterised by complex structural interference between adjacent teeth, was used. Compared with previous methods, this method is more accurate and robust. A local level-set model based on edge features was used to achieve high-precision segmentation of independent teeth. This paper proposes two coefficients for optimising the edge indicator that can adaptively adjust the edge indicator weights based on different structures at the tooth boundary. In the case of close contact between the root and alveolar bone caused by tooth rotation and displacement, the level-set curve can be guided to evolve to the actual tooth boundary, achieving precise differentiation between the two. The experimental results showed that the average Dice similarity coefficient values for the incisors, canines, premolars, and molars were 93.30%, 93.47%, 93.24%, and 93.89%, respectively. The tooth centroids were 0.66, 0.61, 0.87, and 0.80 mm, respectively, using the method proposed in this study. In addition, this method is simple and effective, without relying on many annotated datasets, and a complete 3D dental model with high accuracy and stability can be constructed, which will benefit computer-aided dental treatment.

Ethics statement

This study was approved by the Academic Committee of Changchun University of Science and Technology for Medical Experimental Ethics with ethical approval number 0002.

Data availability statement

Due to the nature of this research, participants in this study did not consent to the public sharing of their data. Therefore, supporting data is not available.

Funding statement

CRediT authorship contribution statement

Shuyi Jiang: Writing – review & editing, Writing – original draft, Validation, Software, Methodology, Formal analysis, Data curation, Conceptualization. **Han Zhang:** Visualization, Validation, Supervision, Software, Resources, Formal analysis, Data curation. **Zhi Mao:** Writing – review & editing, Visualization, Validation, Supervision, Software, Resources, Project administration, Investigation, Formal analysis, Data curation. **Yonghui Li:** Visualization, Validation, Supervision, Software, Project administration, Investigation, Formal analysis, Data curation, Conceptualization. **Guanyuan Feng:** Writing – review & editing, Visualization, Validation, Supervision, Project administration, Investigation, Funding acquisition, Formal analysis, Data curation, Conceptualization.

Declaration of competing interest

The authors declare the following financial interests/personal relationships which may be considered as potential competing interests:Guanyuan Feng reports financial support was provided by Jilin Provincial Science and Technology Department. If there are other authors, they declare that they have no known competing financial interests or personal relationships that could have appeared to influence the work reported in this paper.

References

[1] F.L. Herren, V. Gerber, R. Meier, D. Schweizer-Gorgas, M.D. Klopfenstein Bregger, Semi-automatic segmentation of cone beam computed tomography datasets for volume measurements of equine cheek teeth, J. Vet. Dent. 39 (1) (2022 Mar) 41–48, https://doi.org/10.1177/08987564211061630. Epub 2021 Dec 6. PMID: 34866465.

[2] V. Ronsivalle, P. Venezia, M. Migliorati, C. Grippaudo, E. Barbato, L. Nucci, G. Isola, R.M. Leonardi, A. Lo Giudice, Accuracy of imaging software for 3d rendering of tooth structures, useable in clinical settings, Int. J. Comput. Dent. (2023 Jun 5), https://doi.org/10.3290/j.ijcd.b4140897. Epub ahead of print. PMID: 37272346.

[3] M.L. Poleti, T.M. Fernandes, O. Pagin, M.R. Moretti, I.R. Rubira-Bullen, Analysis of linear measurements on 3D surface models using CBCT data segmentation obtained by automatic standard pre-set thresholds in two segmentation software programs: an in vitro study, Clin. Oral Invest. 20 (1) (2016 Jan) 179–185, https://doi.org/10.1007/s00784-015-1485-5. Epub 2015 May 13. PMID: 25963719.

[4] H. Akhoondali, R. Zoroofi, G. Shirani, Rapid automatic segmentation and visualization of teeth in CT-scan data, J. Appl. Sci. 9 (2009) 2031–2044, https://doi.org/10.3923/JAS.2009.2031.2044.

[5] Y. Gan, Z. Xia, J. Xiong, Q. Zhao, Y. Hu, J. Zhang, Toward accurate tooth segmentation from computed tomography images using a hybrid level set model, Med. Phys. 42 (1) (2015) 14–27, https://doi.org/10.1118/1.4901521.

[6] Sh Keyhaninejad, R.A. Zoroofi, S.K. Setarehdan, Shirani Gh, Automated segmentation of teeth in multi-slice CT images, in: Proceedings of the IET International Conference on Visual Information Engineering, 2006, pp. 339–344.

[7] M. Hosntalab, R. Aghaeizadeh Zoroofi, A. Abbaspour Tehrani-Fard, G. Shirani, Segmentation of teeth in CT volumetric dataset by panoramic projection and variational level set, Int. J. Comput. Assist. Radiol. Surg. 3 (2008) 257–265, https://doi.org/10.1007/s11548-008-0208-7.

[8] H. Heo, O. Chae, Segmentation of tooth in CT images for the 3D reconstruction of teeth, in: Proceedings of SPIE-IS&T Electronic Imaging, 2004, pp. 455–466.

[9] X. Wu, H. Chen, Y. Huang, H. Guo, T. Qiu, L. Wang, Center-sensitive and boundary-aware tooth instance segmentation and classification from cone-beam CT, in: 2020 IEEE 17th International Symposium on Biomedical Imaging (ISBI), 2020, pp. 939–942.

[10] Z. Cui, B. Zhang, C. Lian, C. Li, L. Yang, W. Wang, et al., Hierarchical morphology-guided tooth instance segmentation from cbct images, in: International Conference on Information Processing in Medical Imaging, Springer, 2021, pp. 150–162.

[11] T.J. Jang, K.C. Kim, H.C. Cho, J.K. Seo, A fully automated method for 3D individual tooth identification and segmentation in dental CBCT, IEEE Trans. Pattern Anal. Mach. Intell. 44 (10) (2022) 6562–6568, https://doi.org/10.1109/TPAMI.2021.3086072.

[12] Y. Yang, R. Xie, W. Jia, Z. Chen, Y. Yang, L. Xie, et al., Accurate and automatic tooth image segmentation model with deep convolutional neural networks and level set method, Neurocomputing 419 (2021) 108–125, https://doi.org/10.1016/j.neucom.2020.07.110.

[13] S. Lee, S. Woo, J. Yu, J. Seo, J. Lee, C. Lee, Automated CNN-based tooth segmentation in cone-beam CT for dental implant planning, IEEE Access 8 (2020) 50507–50518, https://doi.org/10.1109/ACCESS.2020.2975826.

[14] P. Lahoud, M. EzEldeen, T. Beznik, H. Willems, A. Leite, A. Van Gerven, et al., Artificial intelligence for fast and accurate 3-dimensional tooth segmentation on cone-beam computed tomography, J. Endod. 47 (5) (2021) 827–835, https://doi.org/10.1016/j.joen.2020.12.020.

[15] Z. Cui, Y. Fang, L. Mei, B. Zhang, B. Yu, J. Liu, et al., A fully automatic AI system for tooth and alveolar bone segmentation from cone-beam CT images, Nat. Commun. 13 (1) (2022) 2096, https://doi.org/10.1038/s41467-022-29637-2.

[16] W. Ge, S. Yang, Y. Yu, Multi-evidence filfiltering and fusion for multi-label classi-fification, object detection and semantic segmentation based on weakly super-vised learning, in: Proceedings of the IEEE Conference on Computer Vision and Pattern Recognition, 2018, pp. 1277–1286.

[17] D. Zhang, H. Zhang, J. Tang, X. Hua, Q. Sun, Causal intervention for weakly–supervised semantic segmentation, in: Proceedings of the Advances in Neural Information Processing Systems, 2020, pp. 1–8.

[18] H. Gao, O. Chae, Individual tooth segmentation from CT images using level set method with shape and intensity prior, Pattern Recogn. 43 (2010) 2406–2417, https://doi.org/10.1016/j.patcog.2010.01.010.

[19] Z. Xia, Y. Gan, L. Chang, J. Xiong, Q. Zhao, Individual tooth segmentation from CT images scanned with contacts of maxillary and mandible teeth, Comput. Methods Progr. Biomed. 138 (2017) 1–12, https://doi.org/10.1016/j.cmpb.2016.10.002.

[20] S. Liu, Y. Wang, A tooth cone beam computer tomography image segmentation method based on the local Gaussian distribution fitting, J. Biomed. Eng. 36 (2) (2019) 291–297, https://doi.org/10.7507/1001-5515.201709042.

[21] Y. Gan, Z. Xia, J. Xiong, G. Li, Q. Zhao, Tooth and alveolar bone segmentation from dental computed tomography images, IEEE J. Biomed. Health Informat. 22 (2018) 196–204, https://doi.org/10.1109/JBHI.2017.2709406.

[22] H.T. Yau, T.J. Yang, Y.C. Chen, Tooth model reconstruction based upon data fusion for orthodontic treatment simulation, Comput. Biol. Med. 48 (2014) 8–16, https://doi.org/10.1016/j.compbiomed.2014.02.001.

[23] D.X. Ji, S.H. Ong, K.W. Foong, A level-set based approach for anterior teeth segmentation in cone beam computed tomography images, Comput. Biol. Med. 50 (2014) 116–128, https://doi.org/10.1016/j.compbiomed.2014.04.006.

[24] C. Li, C.Y. Kao, J.C. Gore, Z. Ding, Minimization of region-scalable fitting energy for image segmentation, IEEE Trans. Image Process. 17 (10) (2008) 1940–1949, https://doi.org/10.1109/tip.2008.2002304.

[25] T. Chan, S. Esedoglu, M. Nikolova, Algorithms for finding global minimizers of image segmentation and denoising models, SIAM J. Appl. Math. 66 (5) (2006) 1632–1648, https://doi.org/10.1137/040615286.

[26] T.F. Chan, L.A. Vese, Active contours without edges, IEEE Trans. Image Process. 10 (2001) 266–277, https://doi.org/10.1109/83.902291.

[27] Y. Jing, J. Liu, Z. Liu, H. Cao, Fast edge detection approach based on global optimization convex model and split Bregman algorithm, Diagnostyka 19 (2) (2018) 23–29, https://doi.org/10.29354/diag/85429.

[28] S. Osher, M. Burger, D. Goldfarb, J. Xu, W. Yin, An iterative regularization method for total variation-based image restoration, Multiscale Model. Simul. 4 (2005) 460–489, https://doi.org/10.1137/040605412.

[29] Z. Xia, Y. Gan, J. Xiong, Q. Zhao, J. Chen, Crown segmentation from computed tomography images with metal artifacts, IEEE Signal Process. Lett. 23 (5) (2016) 678–682, https://doi.org/10.1109/LSP.2016.2545702.

[30] V. Caselles, R. Kimmel, G. Sapiro, Geodesic active contours, Int. J. Comput. Vis. 22 (1) (1997) 61–79, https://doi.org/10.1109/ICCV.1995.466871.

[31] Y. Wang, S. Liu, G. Wang, Y. Liu, Accurate tooth segmentation with improved hybrid active contour model, Phys. Med. Biol. 64 (1) (2018), 015012, https://doi.org/10.1088/1361-6560/aaf441.

[32] M. Quan, Q. Liu, X. Chen, X. Deng, K. He, Y. Liu, Application of an improved geodesic activity contour model in kidney CT image segmentation, China Org. Eng. Res. (in Chinese) 27 (2) (2023) 171–176, https://doi.org/10.12307/2022.945.

[33] Z. Zhu, S. Yan, Y. Ruan, B. Han, Prostate MR image segmentation based on an improved DRLSE model, J. Spectroscopy (in Chinese) 37 (4) (2020) 447–455, https://doi.org/10.11938/cjmr20192786.

[34] K. Zhang, H. Song, L. Zhang, Active contours driven by local image fitting energy, Pattern Recogn. 43 (4) (2010) 1199–1206, https://doi.org/10.1016/j.patcog.2009.10.010.

[35] R. Xie, Y. Yang, Z. Chen, WITS: weakly-supervised individual tooth segmentation model trained on box-level labels, Pattern Recogn. 133 (2023), https://doi.org/10.1016/j.patcog.2022.10897.

[36] Z. Ji, Y. Xia, Q. Sun, G. Cao, Q. Chen, Active contours driven by local likelihood image fitting energy for image segmentation, Inf. Sci. Int. J. 301 (2015) 285–304, https://doi.org/10.1016/j.ins.2015.01.006.